arXiv:1512.07668v1 [cond-mat.soft] 23 Dec 2015

Liquid morphologies and capillary forces between three spherical beads

Ciro Semprebon[1], Mario Scheel[1,2], Stephan Herminghaus[1], Ralf Seemann[1,3], and Martin Brinkmann[1,3]
(1) Max-Planck-Institute for Dynamics and Self-Organization, Am Fassberg 7, D-37077 Göttingen, Germany
(2) Synchrotron Soleil, LOrme des Merisiers, Saint-Aubin, F-91192 Gif-sur-Yvette, France and
*(3) Experimental Physics, Saarland University, D-66123 Saarbrücken, Germany**
(Dated: December 25, 2015)

Equilibrium shapes of coalesced pendular bridges in a static assembly of spherical beads are computed by numerical minimization of the interfacial energy. Our present study focuses on generic bead configurations involving three beads, one of which is in contact to the two others while there is a gap of variable size between the latter. In agreement with previous experimental studies, we find interfacial 'trimer' morphologies consisting of three coalesced pendular bridges, and 'dimers' of two coalesced bridges. In a certain range of the gap opening we observe a bistability between the dimer and trimer morphology during shrinking and growth. The magnitude of the corresponding capillary forces in presence of a trimer or dimer depends, besides the gap opening only on the volume or Laplace pressure of liquid. For a given Laplace pressure, the capillary forces in presence of a trimer are slightly larger than the force of a single bridges at the same gap opening, which could explain the shallow maximum and plateau of the capillary cohesion of a wetting liquid for saturations in the funicular regime.

I. INTRODUCTION

Capillary forces and the mechanics of wet granular materials have remained an active field of research since the seminal works of Haines [1] and Fisher [2] on soil mechanics. Most models consider capillary forces in the presence of cylindrically symmetric pendular bridges [3–8], and are thus restricted to the describe the mechanics at low liquid saturations [9, 10]. Recent developments in three dimensional imaging techniques such as fast confocal microscopy [11] and X-ray tomography [12] made it possible to investigate the shape of liquid clusters in the funicular regime with a resolution well below the scale of a single grain. Despite these advances, only a few attempts have been made to quantify capillary forces in the funicular regime [12–14]. It is evident that the magnitude of the cohesive forces at different liquid saturations is intimately linked to the morphology of the interstitial fluids on the scale of single grains [12, 15]. A better understanding of the liquid structures emerging in the funicular regime and the capillary cohesion caused by them may help to predict landslides or avalanches [16], and to complement existing models for technological applications in wet aggregation or particle coating [17]. Besides the mechanics of wet granulates, modeling the cluster morphology of partially wetting liquids will also have repercussions on the theory of fluid transport in wet granular beds [10, 15, 18–20].

In this article we present the results of a systematic study of fundamental liquid morphologies and corresponding capillary forces in arrangements of spherical beads beyond the regime of pendular bridges. These clusters appear at liquid saturations corresponding to the transition form the pendular to funicular regime. Considering perfectly wetting liquids and a random close packing of spherical beads, the pendular bridge regime is limited to a range of liquid content $W < W^* \approx 2.5 \cdot 10^{-2}$, here expressed with respect to the total sample volume [12, 21]. At slightly higher liquid contents $W > W^*$, the lateral extension of a pendular bridges on the bead surface does not anymore permit the formation of isolated bridges. Consequently, a certain fraction of the pendular bridges coalesces and transforms into a funicular structure, i.e. into liquid clusters that are simultaneously in contact to at least three beads.

The most characteristic cluster morphology found in granular bed of highly wettable spherical beads is a 'trimer' of pendular bridges [12]. As can be seen in the three dimensional rendering of x-ray tomography data in Fig. 1 (a), [12] three pendular bridges have coalesced around a triangular opening formed by three adjacent beads. In what follows we refer to the center of the opening as a 'throat'. Throats are found in large numbers in a disordered assembly of spherical beads [12, 22], and it is not surprising that filled throats connecting three adjacent bridges represent the most generic liquid structure beyond isolated pendular bridges. A close inspection of the liquid morphology shown in Fig. 1 (c) reveals that this large liquid cluster indeed consists mostly of these trimer units: Any of the three pendular bridges belonging to a certain trimer unit can be part of a least one more trimer unit. The filled throats in a granular assembly can thus form large interconnected chains of pendular bridge 'polymers'. Owing to its outstanding importance we will focus our present numerical study on a single trimer.

Capillary forces of pendular bridges between two spherical beads in contact display only small variations with the liquid volume [2, 14, 16]. This observation

* martin.brinkmann@physik.uni-saarland.de

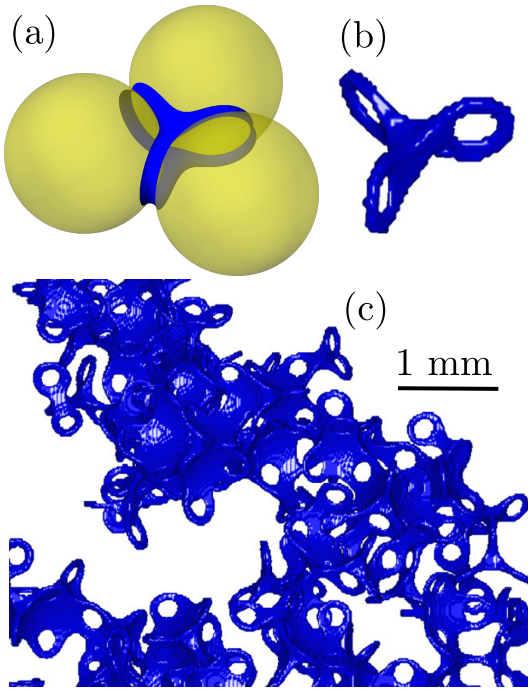

FIG. 1. (Color online) (a): Trimer morphology computed in our numerical energy minimizations. (b) and (c): Renderings of segmented X-ray mircotomography images of a wetting liquid between spherical glass beads and a large liquid cluster in a disordered packing from x-ray tomography [12]. Bead radius $R = (355 \pm 35)\mu$m, wetting liquid aqueous ZnI_2 solution in (b) and (c).

readily explains the insensitivity of the mechanical cohesion of a wet granular assembly with respect to the liquid content W in the pendular regime $W \lesssim W^*$ [16]. Quite surprisingly, the magnitude of capillary cohesion evolves smoothly while the liquid content is increased from the pendular regime $W \lesssim W^*$ into the funicular regime $W \gtrsim W^*$ [12]. Measurements of capillary cohesion employing the fluidization threshold or the tensile strength [9, 12] reveal a plateau in the range of W from approximately 0.03 reaching to values larger than ≈ 0.1. At higher liquid contents, capillary cohesion gradually weakens with increasing W and vanishes at full saturation of the pore space ($W \approx 0.4$). In the latter case, every bead in the granular bed is completely immersed in liquid and, thus, there are no fluid interfaces that can give rise to capillary cohesion.

An experimental quantification of capillary forces in small ensembles of beads is difficult and *in situ* measurements are hardly feasible with the currently available experimental techniques. To reach a quantitative picture of capillary cohesion between three or more beads, we employ numerical minimizations of the interfacial free energy and obtain the equilibrium morphology of the liquid interfaces along with the magnitude and direction of capillary forces. The respective capillary forces as a function of the surface–to–surface separations can be then employed to formulate a model for the mechanics of wet beads, provided the complete set of rules to transform, merge, or split liquid cluster in response to slow changes of the local bead configuration is known [15].

A statistical analysis of X-tomography images revealed that local triangular configurations with three detectable finite separations between the bead surfaces are extremely rare in random packings of monodisperse beads [12, 20]. The majority of these local 'throats' exhibit only one detectable gap between the surfaces of the beads. The beads of the remaining two pairs are in mechanical contact. The other extreme case where all three bead pairs are in contact is equally rare. Significant differences in the statistics of surface-to-surface separations of adjacent beads between dry and wet assemblies could be detected in the X-ray tomography [12]. In view of the three dimensional parameter space that accounts for the most general configurations of three beads, we will restrict our discussion in this work to the most relevant case, i.e. three bead configurations with two mechanical contact and one finite gap opening. To account for the range of experimentally relevant situations we report the results for both the volume controlled case and the pressure control case. Local bead configurations where all three pairs are in contact are covered as a special case. In a forthcoming work, we will present the results on the general case with two and three finite gap openings, respectively.

This article is organized as follows: In Sec. II we introduce the physical model and give details about the numerical method to compute equilibrium configurations of the liquid interface. In Sec. II, we summarize the fundamentals of theory of capillarity and methods to compute capillary forces between solid bodies in numerical energy minimizations. The appearance of trimers and dimers of pendular bridges in local bead configurations with two contacts are described in Sec. III A and compared to wetting experiments in Sec. III B. Numerically computed capillary forces between beads in the presence of trimers and dimers are presented and discussed in Sec. III C. Finally, we conclude with a summary and outlook in Sec. IV.

II. PHYSICAL MODEL AND NUMERICAL IMPLEMENTATION

Before we address the theory of capillary forces, we will first give a short outline of the framework of capillarity. To this end, we will consider the most general case of N spherical beads in contact to two fluid phases. The position of the N bead centers are given by vectors $\mathbf{r}_1, \mathbf{r}_2, ..., \mathbf{r}_N$ with Cartesian coordinates $\mathbf{r}_i = (x_i, y_i, z_i)$. For later convenience we denote vectors and tensors by boldface symbols. The fluid phases in contact to the beads may represent two immiscible liquids or a liquid in coexistence with a vapor phase. As we assume the beads to be fixed in space, or allowing only adiabatically

slow variations of their positions, any flow inside the fluid phases has ceased once a mechanical equilibrium of the bulk phases and their interfaces has been reached. In this state, both fluids are at rest relative to the surface of the beads which implies the absence of viscous stresses.

A. Interfacial energies

The shape of the liquid-vapor interface in mechanical equilibrium and the corresponding capillary forces and torques acting on the beads can be obtained from thermodynamic considerations of the interfacial free energy $\mathcal{E}$. For given positions $\mathbf{r} \equiv (\mathbf{r}_1, \mathbf{r}_2, ..., \mathbf{r}_N)$ of the bead centers, the functional

$$\mathcal{E}\{\Sigma^{\mathrm{lv}}\} = \gamma^{\mathrm{lv}} A^{\mathrm{lv}} + \left(\gamma^{\mathrm{ls}} - \gamma^{\mathrm{vs}}\right) \sum_{i=1}^{N} A_i^{\mathrm{ls}} \tag{1}$$

assigns a free energy to every configuration Σ^{lv} of the liquid-vapor interface. The first term on the RHS of eqn. (1) represents the free energy of the liquid-vapor interface with area A^{lv} and interfacial tension γ^{lv}. The second term in eqn. (1) accounts for the free energy related to the surface Σ_i^{ls} of bead i in contact to the liquid with area $A_i^{\mathrm{ls}} \equiv |\Sigma_i^{\mathrm{ls}}|$ and the liquid-solid and vapor-solid surface tension γ_{ls} and γ_{vs}, respectively.

Throughout this work, we will neglect the influence of gravity and buoyancy, as their effects are typically small in liquid clusters with extensions on the length scale of the grains. The capillary length for an air water interface is in the range of a few millimeters [23]. Expressed in terms of the Bond number $\mathsf{Bo} \equiv \Delta\rho\, g R^2/\gamma^{\mathrm{lv}}$ with a typical vertical dimension of the interface in the range of the bead radius, we have $\mathsf{Bo} \ll 1$. Furthermore, we assume that the typical distances between the liquid interface and solid walls are large such that contributions of the disjoining pressure to the normal stress at the interface can be safely excluded.

Under these conditions, any mechanically stable interface configuration Σ^{lv} in contact to the beads with fixed positions $\bar{\mathbf{r}}$, is a local minimum of the free energy eqn. (1). Dealing with non-volatile liquids, we have to consider minima of the functional (1) under the subsidiary constraint of a fixed volume V of the liquid body. We will refer to this situations as the 'volume controlled case'.

In some situations it is justified to assume that the liquid in contact to the beads can be exchanged with a reservoir that fixes the pressure difference $P \equiv P^{\mathrm{l}} - P^{\mathrm{v}}$ between the liquid (l) and vapor (v) phase. If this is the case we have to find local minima of the Grand interfacial free energy

$$\mathcal{G} = \mathcal{E} - P V \ , \tag{2}$$

The grand interfacial free energy takes into account the work received from or done at the volume reservoir, respectively. We will refer to this case as the 'pressure controlled case'.

Any extremum of the free energy $\mathcal{E}$ under the constraint of a fixed volume V necessarily satisfies two conditions. The first condition is expressed by the Young-Laplace equation:

$$P = 2H\gamma^{\mathrm{lv}} \ , \tag{3}$$

that holds in every point of the interface Σ_{lv}. The mean curvature H is the sum of the two principal curvatures, or any pair of normal curvatures of the interface into orthogonal direction, see for instance Ref. [24]. In the absence of gravity, the Laplace pressure P is independent on the position which implies that Σ^{lv} is a surface of constant mean curvature.

The second necessary condition of a local free energy minimum is due to Young, Dupré, and Laplace and expresses the mechanical equilibrium at every point the three phase contact line:

$$\gamma^{\mathrm{lv}} \cos\theta_0 = \gamma^{\mathrm{sv}} - \gamma^{\mathrm{sl}} \ . \tag{4}$$

The equilibrium contact angle θ_0, also termed Young's or material contact angle, is determined solely by interfacial free energies. For comparison to 'real' experimental systems, we have to consider static advancing and static receding contact angles instead of Young's angle θ_0 to account for the dissipation of work during and advancing or receding motion of the three phase contact line on a heterogeneous surface.

Owing to inherent non-linearity of the energy functional eqn. (1), the interfacial free energy $\mathcal{E}$ may exhibit more than a one local extremum for a given liquid volume V and given positions $\bar{\mathbf{r}}$ of the beads. The equilibrium shapes can be distinguished by suitable order parameter describing the interfacial shape. The free energy $\mathcal{E}$ of these equilibrium shapes is a function $E(\bar{\mathbf{r}}, V)$ in a certain range of bead coordinates $\bar{\mathbf{r}}$ and liquid volume V.

In the many instances one finds multiple local minima for given positions $\bar{\mathbf{r}}$, volume V, and material contact angle θ_0. In this case, the function $E(\bar{\mathbf{r}}, V)$ is multi-valued and forms a number of branches (or 'leafs'). Analogous statements hold for the Grand free energy $\mathcal{G}$ and the corresponding energy landscape $G(\bar{\mathbf{r}}, P)$, where the Laplace pressure P represents the accessible control parameter, instead of the liquid volume V.

Any interfacial configuration that satisfies eqns. (3) and (4) is a extremum of the interfacial energy $\mathcal{G}$ for the given Laplace pressure P in eqn. (3). From this observation we can conclude that an extremum of the free energy eqn. (1) for a certain volume V is also an extremum of the Grand free energy eqn. (2) for a certain pressure P and vice versa. This implies that the set of interfacial equilibria in the volume controlled case and in the pressure controlled case are identical. The mechanical stability of these extrema, however, may differ between the volume and the pressure controlled cases. Apart from a constant, the free energies $\mathcal{G}$ and $\mathcal{E}$ are identical for all interfacial configurations enclosing the same volume V. Hence, any local minimum of $\mathcal{G}$ will be also a local minimum of $\mathcal{E}$,

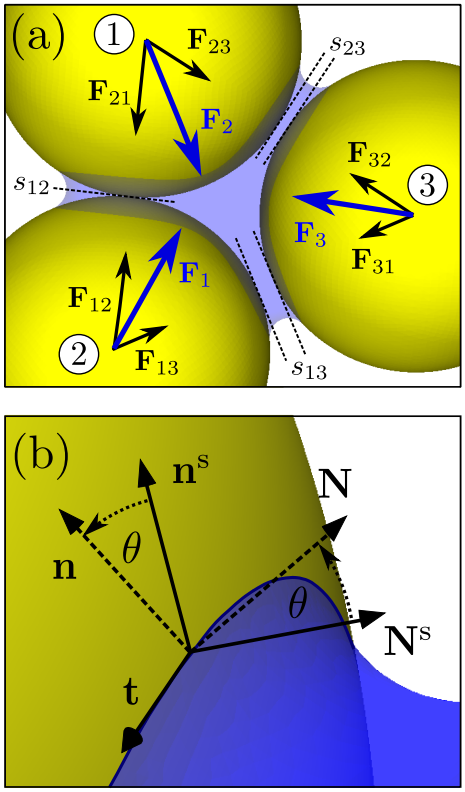

FIG. 2. (Color online) (a): Geometry of three spherical beads with arbitrary gap openings s_{ij}, $i \neq j \in \{1,2,3\}$. The total capillary force $\mathbf{F}_i$ acting on sphere i (blue arrows) is decomposed into force pairs acting along the line joining the bead centers (black arrows). (b):Local orthonormal vector bases in a point $\mathbf{r}$ of the contact line Γ_i of a liquid-vapor interface Σ^{lv} on the surface Σ_i^{s} of beads i. Here, $\mathbf{t}$ denotes the tangent to Γ_i, $\mathbf{N}_s$ the normal of Σ_i^{s}, $\mathbf{N}$ the normal of Σ^{lv}, θ the contact angle, while $\mathbf{n}$ and $\mathbf{n}^{\mathrm{s}}$ denote the outward pointing co-normal vectors of Σ^{lv} and Σ^{ls}, respectively.

where the Laplace pressure P in $\mathcal{G}$ can be regarded as a Lagrange multiplier to enforce the constraint of a constant liquid volume V. Mechanical stability in the pressure controlled case always implies mechanical stability in the volume controlled case. The converse statement, however, is not necessarily true: the liquid may exhibit more locally stable states in the volume controlled case as compared to the pressure controlled case.

At specific values of the relevant control parameters liquid volume V or Laplace pressure P and bead configuration $\bar{\mathbf{r}}$, termed 'bifurcation points', the number of local minima and saddle points of the energy functionals $\mathcal{E}$ and $\mathcal{G}$ changes. Bifurcation points can be classified according to universal aspects of the underlying energy landscape, i.e. the number of control parameters and order parameters as well as the symmetries of the energy functionals is the subject of catastrophe theory, cf. Refs. [25, 26].

B. Capillary forces

The interfacial free energy $E(\bar{\mathbf{r}}, V)$ of a branch of liquid equilibrium states can be employed to compute the capillary force acting on the beads. Besides a negative sign, the total force $\mathbf{F}_i$ acting on bead i can be obtained from a gradient

$$\mathbf{F}_i = -\nabla_{\mathbf{r}_i} E(\bar{\mathbf{r}}, V) \ , \tag{5}$$

with respect to the Cartesian coordinates $\mathbf{r}_i$ of the particles $i \in \{1, 2, ..., N\}$.

Capillary forces are unique for the equilibrium conformation of the liquid in contact to the beads, and do not depend on whether the liquid volume or the pressure is considered as the controlled parameter. Whenever $\partial_V \tilde{P}(\bar{\mathbf{r}}, V) \neq 0$, we can find the inverse function $V = \tilde{V}(\bar{\mathbf{r}}, P)$ for given bead positions $\bar{\mathbf{r}}$, where we use the tilde to distinguish the variable from the respective function. As shown in the appendix IV A, we can derive the identity

$$\nabla_{\mathbf{r}_i} G\big(\bar{\mathbf{r}}, P\big) = \nabla_{\mathbf{r}_i} E\big(\bar{\mathbf{r}}, V\big)|_{V=\tilde{V}(\bar{\mathbf{r}},P)} \ , \tag{6}$$

expressing that the capillary forces in a mechanical equilibrium are the same in the volume controlled case and the pressure controlled case, provided we consider corresponding values of the volume V and the Laplace pressure P. Higher derivatives of $E(\bar{\mathbf{r}}, V)$ and $G(\bar{\mathbf{r}}, P)$ with respect to the coordinates $\bar{\mathbf{r}}$ (evaluated at a Laplace pressure $P = \tilde{P}(\bar{\mathbf{r}}, V)$), however, differ in the general case.

Once the interfacial energies $\tilde{E}(\bar{\mathbf{r}}, V)$ or $\tilde{G}(\bar{\mathbf{r}}, P)$ are known, we can derive the capillary force $\mathbf{F}_i$ from partial derivatives of with respect to the Cartesian coordinates $r_{i\alpha}$, $\alpha \in \{x, y, z\}$ for every bead i. This approach is numerically costly because one needs to first scan a high dimensional function over a large range of parameter. Calculating the capillary forces directly from the configuration Σ^{lv} of the interface in a local minimum of $\mathcal{E}$ or $\mathcal{G}$, respectively, involves integrations over the three phase contact line of the interface which is much less costly.

To determine the total capillary force acting on each single bead, let us first imagine that every bead is enclosed by a control surface. This virtual control surface shall be infinitesimally close to the bead surface. By definition, the control surface must not intersect with any of the adjacent beads. Integration of the normal component of the stress tensor over the control surface yields the total capillary force on a bead. The magnitude and direction of this force is independent on the particular choice of the control surface.

The the total capillary force $\mathbf{F}_i$ acting on bead $i = 1, 2, 3$ can be split into a contribution of the isotropic pressure in the liquid and ambient fluid (index p) and a contribution that stems from the interfacial tension (index t):

$$\mathbf{F}_i = \mathbf{F}_i^{\mathrm{p}} + \mathbf{F}_i^{\mathrm{t}} \ . \tag{7}$$

The first contribution $\mathbf{F}_i^{\mathrm{p}}$ is given by the Laplace pressure $P \equiv P^{\mathrm{l}} - P^{\mathrm{v}}$ multiplied by the local surface normal $\mathbf{N}^{\mathrm{s}}$ of the solid, and integrated over the surface Σ_i^{ls} of the bead i in contact to the liquid:

$$\mathbf{F}^{\mathrm{p}} = \int_{\Sigma_i^{\mathrm{ls}}} \mathrm{d}A \, P \, \mathbf{N}^{\mathrm{s}} \; . \tag{8}$$

Note, that this contribution to the capillary force vanishes if the bead is completely immersed in the liquid provided that P is constant.

The second contribution $\mathbf{F}_i^{\mathrm{t}}$ arises only in the presence of a three phase contact line Γ_i on the bead i, i.e. if bead i is partially wet. Locally, the interfacial tension γ^{lv} of the liquid-vapor interface Σ^{lv} pulls into a direction perpendicular to both the tangent vector $\mathbf{t}$ of the contact line Γ_i, and the local normal vector $\mathbf{N}$ of Σ^{lv} in a point $\mathbf{r}$ on Γ_i, which is expressed as a force per unit length

$$\mathbf{f} = \gamma^{\mathrm{lv}} (\mathbf{N}^{\mathrm{s}} \sin\theta - \mathbf{n}^{\mathrm{s}} \cos\theta) \; . \tag{9}$$

The sketch in Fig. 2(b) illustrates the definition of the two local orthonormal vector bases $\{\mathbf{t}, \mathbf{N}, \mathbf{n}\}$ of the liquid vapor interface Σ^{ls} and $\{\mathbf{t}, \mathbf{N}^{\mathrm{s}}, \mathbf{n}^{\mathrm{s}}\}$ on the surface Σ^{s} of the bead, as well as the local contact angle θ between Σ^{ls} and Σ^{s} in a point $\mathbf{r} \in \Gamma_i$. The surface normal of the free interface, $\mathbf{N}$, and the local normal of the bead surface, $\mathbf{N}^{\mathrm{s}}$, allow us to express the local contact angle as

$$\cos\theta = \mathbf{N} \cdot \mathbf{N}^{\mathrm{s}} \; . \tag{10}$$

The vectorial line force eqn. (9) integrated over the contact line Γ_i on bead i yields the total force that the liquid-vapor interface exerts on bead i:

$$\mathbf{F}_i^{\mathrm{t}} = \int_{\Gamma_i} \mathrm{d}\ell \, \mathbf{f}(\mathbf{r}) \; . \tag{11}$$

In our numerical energy minimizations, integrals of eqn. (9) over the contact line can be performed as summations over the corresponding expressions at the edges representing the contact line. Employing the divergence theorem, one can re-express the surface integral in eqn. (8) by line a integral over suitable functions.

In the remainder of this article, we will consider the ideal case of a homogeneous bead surfaces where the local contact angle is identical to Young's angle θ_0 as given by eqn. (4).

C. Numerical implementation

Due to a lack of high symmetries like, e.g. the rotational symmetry, the computation of the equilibrium shapes of liquid volume wetting three spheres can be achieved only by means of numerical methods. In this work we employ a numerical minimization of the interfacial energy with the freely available software Surface Evolver developed by K. Brakke [27]. A fundamental idea behind this method is that the shape a liquid droplet in contact to a rigid substrate is entirely fixed by the configuration of the free liquid-vapor interface.

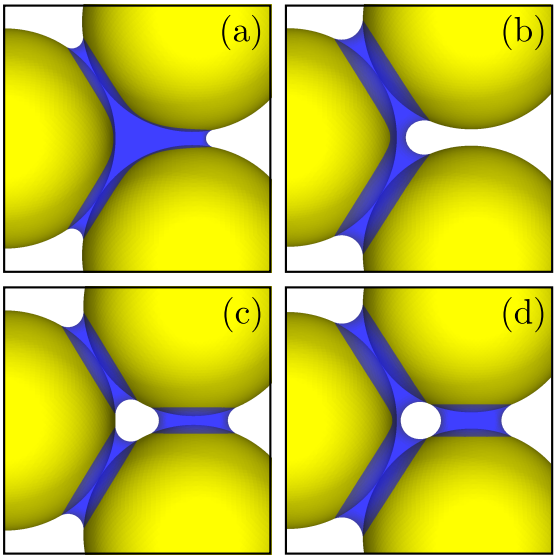

FIG. 3. (Color online) Liquid morphologies in contact to three beads of equal radius with one non-zero gap opening showing (a) a trimer, (b) a dimer, (c) three pendular bridges, and (d) a dimer coexisting with a single pendular bridges.

In the numerical model of the liquid droplet, or droplets in contact to the beads the shape of the liquid-air interface is approximated by a mesh of small triangles spanning a set of nodes. The interfacial energy is a function of the $3N$ coordinates of the nodes, and can be minimized using a number of build in optimization algorithms [27]. Nodes of the mesh which represent the three phase contact line have to glide and stay on the spherical surface of one of the beads. Local geometrical constraint keeps the nodes of the contact line on the surface. Contributions to the interfacial energy which stem from the surface of the beads in contact to the liquid are completely determined by the configuration of the boundary to the liquid-air interface and are numerically computed from line integrals of suitably chosen functions over the closed contact line [27].

During minimization of the interfacial energy, the condition of a constant liquid volume is imposed through a global integral constraint. Provided the configuration is in a local minimum of the interfacial free energy, the Lagrange multiplier corresponding to this integral constraint that has to be calculated in every minimization step is identical to the Laplace pressure P, i.e. the pressure difference across the liquid-air interface. Alternative to the ensemble of interfacial configurations enclosing a constant volume, one may consider an ensemble where the Laplace pressure of the liquid is fixed by a reservoir while the volume is allowed to fluctuate.

A variety of gradient based energy minimizations

schemes including conjugate gradient descent are implemented in the surface evolver. Furthermore, a complete script language allows us to extract geometrical quantities from the liquid-air interface, such the position of special points of the contact line. Long and short edges of the triangulation are refined, respectively, removed from the mesh after a number of minimization steps in order to keep the size distribution of the triangles in a desired range. Subsequent edge flipping allows the mesh to adapt to large changes of the configuration.

Preforming numerical computations of interfacial energies, Laplace pressures, and forces, it is useful to employ dimensionless rescaled physical quantities. For later convenience, we rescaled any length in the system by $L_0 \equiv R$ and express volumes in units of $V_0 \equiv R^3$. Energies will be rescaled by $E_0 \equiv \gamma^{\rm lv} R^2$ and, consequently, capillary forces and the Laplace pressure by a force scale $F_0 \equiv \gamma^{\rm lv} R$ and pressure scale $P_0 \equiv \gamma^{\rm lv}/R$, respectively. For the sake of brevity and to improve the readability of the text, we will from now on speak of the non-dimensional rescaled quantities, if not otherwise mentioned.

III. RESULTS

Throughout this work we consider three identical spherical beads, as illustrated in the sketch of Fig. 2. Assuming a wetting liquid in our numerical energy minimizations wet set the contact angle to $\theta_0 = 5°$. Two of the three bead pairs in the numerical model are in contact, while the third pair exhibits a finite gap. Without losing generality, we chose gap openings $s_{12} > 0$ and $s_{13} = s_{23} = 0$, i.e. bead 1 and 2 are not in mechanical contact. Hence, the two remaining control parameter that define the relative position of the beads are s_{12}, and either the liquid volume V or the Laplace pressure P.

A. Liquid morphologies

Figure 3 presents four mechanically stable interfacial morphologies encountered in our numerical energy minimizations in the volume controlled case. These are the trimer of three coalesced pendular bridges in panel (a) of Fig. 3, a dimer of two coalesced bridges at the contacts in (b), three isolated pendular bridges in (c), and a bridge dimer at the contacts coexisting with a pendular bridge across the gap in (d). Throughout this work we assume that separate liquid bodies can be exchange volume. Consequently, the relevant parameter in the volume controlled case is the total volume of all liquid bodies.

Inspection of the liquid-vapor interface of the dimer and the trimer shows that both interfaces are topologically equivalent to the surface of a sphere perforated by three holes. Despite this similarity, the overall shape of a trimer and dimer are qualitatively different. The liquid of a trimer fills the central opening, or 'throat', formed by the three adjacent beads. In the presence of a dimer, however, the central part of this throat is empty of liquid. Dimer morphologies can thus be described by a pair of pendular bridges that have coalesced in a small section of the contact lines.

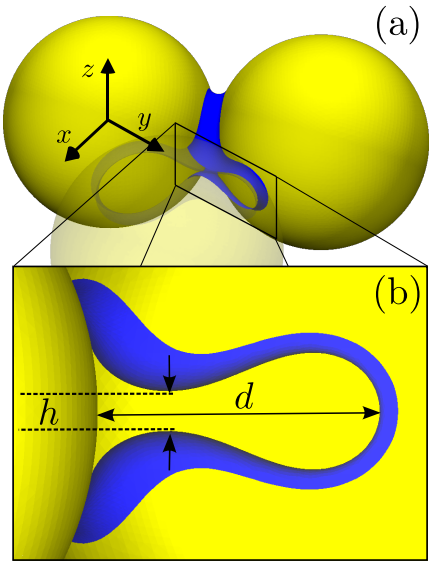

FIG. 4. (a): View of a trimer morphology with liquid volume $V = 0.2$ and material contact angle $\theta_0 = 5°$ wetting a throat of three beads with one finite gap $s_{12} > 0$ and two contacts $s_{13} = s_{23} = 0$. The foremost bead and half of the liquid interface are rendered transparent to enhance the cut along the symmetry plane. (b): Magnified view of a cut through a trimer along its symmetry plane, indicating the definition of the order parameter meniscus distance, d, and the distance h of the two opposing menisci in the throat.

To distinguish the trimer from the dimer morphologies, and to detect certain types of instabilities that occur during quasi-static changes of the control parameter, we consider two suitable shape descriptors as indicated in Fig. 4. Let us imagine a cut through the liquid body by the symmetry plane $x = 0$ orthogonal to the plane $z = 0$ passing through the centers of the spheres. The first shape descriptor is now the distance d between the intersection of liquid interface and the y-axis, and the surface of bead 3, cf. Fig.4. As a second shape descriptor, we chose the smallest distance h of two points on the concave part of the upper and lower meniscus in the throat. This minimum thickness of this 'liquid lamella' may become ill-defined if the meniscus in the throat lack a concave shape, unlike the example shown in Fig. 4.

The plots in Fig. 5 (a) illustrate the evolution of the meniscus distance d as a function of the liquid volume V, for a set of fixed gap opening s_{12} in the range between 0.05 and 0.25. At large a gap opening $s_{12} = 0.25$, we observe a continuous increase of d for an increasing volume V, and no discontinuous jumps. The distance d follows the same curve during a volume decrease and a clear transition between trimer at large V and dimer at

small V cannot be found. Only at small volumes, the trimer/dimer morphology eventually decays, caused by a de-coalescence of the meniscus as $d \to 0$. This interfacial instability, indicated by square symbols in Fig. 5(a), will lead to two separated pendular bridges as a final state.

At smaller gap openings $s_{12} = 0.13, 0.17, 0.21$ the meniscus distance d shown in Fig. 5(a) displays discontinuous jumps to larger or smaller values, depending on whether the volume V is decreased or increased, respectively. Owing to these jumps, we find a range of control parameter s_{12} and V where two branches of local minima of the interfacial free energy (1) can be found in our numerical energy minimizations. This mechanical bistability between a dimer and a trimer allows a clear distinction of the morphologies. The branch of liquid conformations with the larger or smaller value of d are classified as trimers and dimers, respectively. The corresponding interfacial instabilities limiting the range of mechanically stable trimers and dimers will be termed the 'snap–in' and the 'pop–out' instability in the remainder of this article. The latter two instabilities are indicated by downward and upward triangles, respectively, in Fig. 5.

For a gap opening s_{12} of 0.13 and smaller, the snap–in instability occurs at a volume smaller than the smallest volume that allows a stable dimer to be formed, cf. the corresponding branches shown in Fig. 5 (a). Hence, trimers can directly break up into two separated pendular bridges during a volume decrease even without passing through the dimer morphology. For the examples shown in Fig. 5 (a), the trimer branch terminates for a finite value $d > 0$ at gap opening s_{12} of 0.05 and 0.09. In these cases the minimal liquid thickness h in the throat reaches zero before a discontinuous inward jump of the outer meniscus in the gap or a de-coalescence can lead to the decay of the trimer. A collision of the two opposing menisci in the throat triggers a sudden opening of the liquid interfaces. The circles in the plots shown in Fig. 5 (a) and (b) indicate this 'burst' instability during a decreasing liquid volume. The burst instability of the central liquid meniscus very likely leads to three separated pendular bridges as the final state.

Figure 5 (c) illustrates the stability boundaries of the trimer and dimer morphologies that correspond to one of the four possible types of instability. With systematic scans of parameters s_{12} and V, we identified a bifurcation point at $(V^\star, s_{12}^\star) = (0.26, 0.22)$ as indicated by the black star in the stability diagram Fig. 5 (c). The tangents to the lines indicating the snap–in and the pop–out instability become parallel and terminate in a cusp. This type of bifurcation is generically observed for two control parameters and one order parameter, see e.g. Ref. [25, 26]. The lines of the snap–in instabilities and the burst emerge from a point $(V^\blacklozenge, s_{12}^\blacklozenge) = (0.09, 0.125)$, where the two stability lines form a kink. The latter point is indicated by a black diamond in Fig. 5 (c). Note, that mechanically

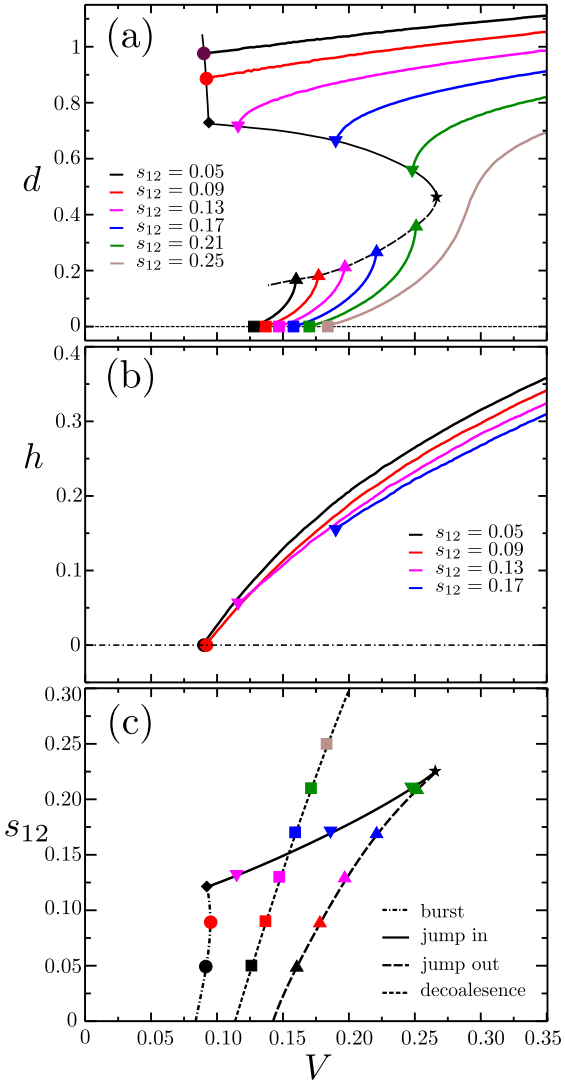

FIG. 5. (Color online) (a): Distance d between the outer meniscus at the gap and the surface of sphere 3 as a function of the volume V for different gap openings s_{12}. (b): Minimal distance h of the two opposing menisci in the throat as function of V for the same values of s_{12}. (c): Morphology diagram in terms of the V and s_{12} displaying the lines of instabilities as outlined in the main text. The bifurcation point and the kink are indicated by the star ($\star$) and diamond ($\blacklozenge$) symbol, respectively. For a definition of d and h, cf. also Fig. 4.

stable dimers can exist in the 'ideal' case $s_{12} = 0$ of all three beads in contact, provided that the volume falls into the narrow range between $V \approx 0.115$ and $V \approx 0.15$.

It turns out that also a mechanically stable 'chimera' morphology of a dimer and an isolated pendular bridge across the finite gap is possible. In contrast to the trimer, the latter morphology is always metastable (a local energy minimum of the interfacial energy) and can found only in a small region of control parameters. As for a single bridge dimer, a volume decrease will likely induce a break-up of the interface between the two coalesced bridges and the formation of three pendular bridges. Al-

ternative to de-coalescence, one may observe that the pendular bridge located at the gap will transfer liquid into the dimer and disappears.

An increase of the liquid volume of the trimer/dimer chimera state, however, will lead to a coalesce of the dimer and the pendular bridge at the gap. The resulting trimer will likely fill the throat opening. Similar to the decay at decreasing volume an increase of the gap opening at fixed volume could induce a rupture of the pendular bridge at the gap. Here, we can speculate that the liquid will first form a transient dimer that finally decays, after a pop–out of the meniscus between the two coalesced bridges, into a trimer.

B. Experiments

Motivated by the results of our numerical energy minimizations in Sec. III A, we investigated the decay of the trimer morphology and the final states during a slow decrease of liquid volume in an experimental realization. To this end, we fix three spherical ruby beads of identical radius $R = (300 \pm 5)\mu$m (purchased from Saphirwerk Industrieprodukte AG and Sandoz Fils Sa, both Switzerland) on a microscopy glass slide using play dough. Two pairs of the beads are in mechanical contact ($s_{13} = s_{23} = 0$) while a small separation is intentionally left between the surfaces of the third pair ($s_{12} > 0$). Deionized water is employed as a volatile wetting liquid with a receding contact angle of $\theta_r \lesssim 10°$ on the surface of the cleaned ruby beads, similar to the material angle of $\theta_0 = 5°$ in our numerical energy minimizations in Sec. III A. In the begining of the experiment a small water droplet is placed in the throat formed by the three ruby beads. During evaporation the shape of the meniscus is recorded by optical microscopy in top view, cf. also Fig. 6(a). Experiments are performed at similar temperatures and relative humidities to ensure comparable evaporation rates.

Examples of video frames of a trimer recorded during a typical evaporation experiment are displayed in Fig. 6(a) for two gap openings. In good agreement with the numerical results of the previous section III A, we observe a burst instability for $s_{12} = 0.115$ (left column) and a discontinuous snap–in at $s_{12} = 0.145$ (right column). The distance of the meniscus in the gap to the surface of the opposing bead is denoted as d, cf. also Fig. 6 (a) and Sec. III A. According to our convention, we rescaled the distance d by the bead radius R.

Figure 6 (b) shows the meniscus distance d extracted from the video frames as a function of time t for a series of gap openings s_{12}. To compare the temporal evolution of d during a snap–in for different values of the gap opening s_{12}, we chose an individual offset on the time axis for each curve in Fig.6 (b) such that the meniscus distance at time $t = 0$ attains the value $d = 0.8$.

Irrespective of the gap opening s_{12}, the meniscus dis-

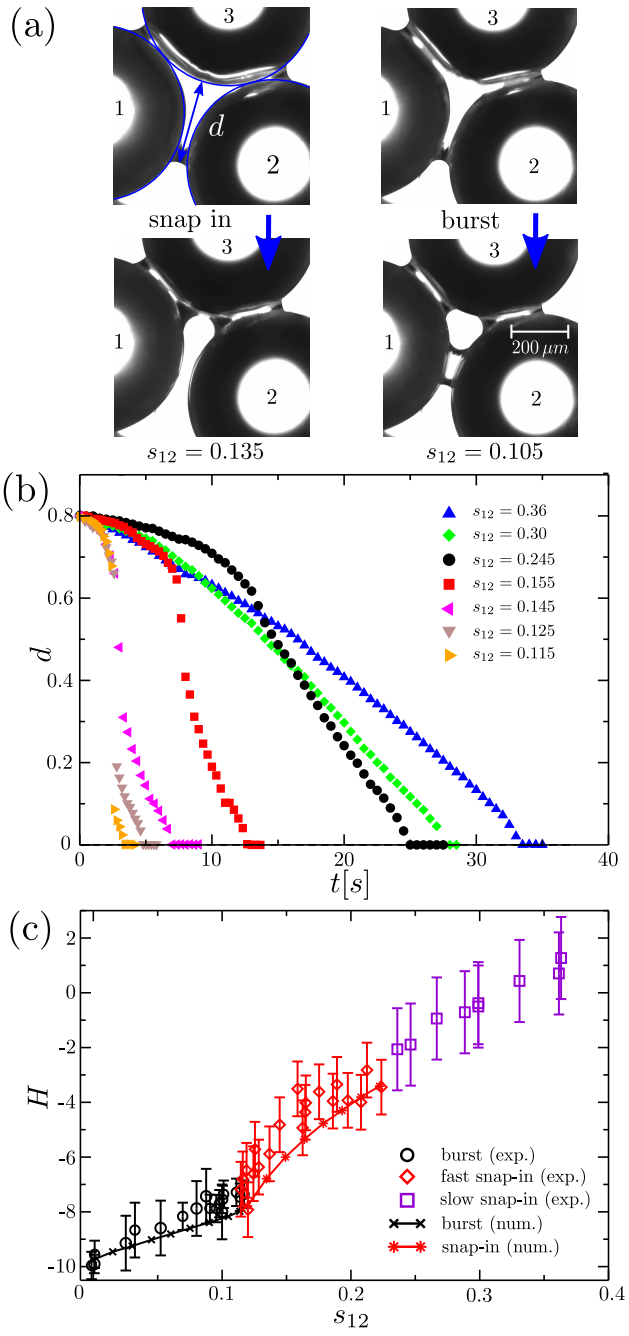

FIG. 6. (Color online) Evaporation of pendular bridge trimer of three water bridges in assembly of three ruby beads with a radius of $R = (300 \pm 5)\mu$m with a finite gap between bead 1 and 2. (a): Optical micrographs of a pendular bridge trimer with a finite gap opening $s_{12} = 0.115$ (top left) and $s_{12} = 0.135$ (top right) and the corresponding final states of the burst instability (left bottom) and snap–in instability (bottom right). (b): Distance d of the outer meniscus in the gap from the surface of the opposing bead as a function of time t elapsed after the meniscus has passed a distance $d = 0.8$ for different gap opening s_{12}. (c): Estimated mean curvature H of an evaporating trimer at the point of instability as a function of the gap opening s_{12} in evaporation experiments and numerical energy minimizations.

tance d is monotonously deceasing as time t passes. The cross-over from a sudden, discontinuous snap–in to a gradual and continuous decrease of d occurs between gap openings s_{12} of 0.155 and 0.245. At this point, we observe also a qualitative change in the form of the functions shown in Fig. 6 (b), which display an increasing s-shape of the curves as s_{12} is decreased. The transition agrees well with the predictions of our numerical energy minimizations in Sec.III A. An expected bifurcation point at a gap opening $s_{12}^{\star} = 0.22$ separates the continuous from the discontinuous trimer decay. The corresponding measured meniscus distance $d^{\star}$ at the expected bifurcation point as well as the values of d at the onset of the snap–in instability for $s_{12} < s_{12}^{\star}$ agree well with the numerically obtained results of Sec. III A shown in Fig. 5.

The snap–in instability was not observed in our evaporation experiments at gap openings $s_{12} \lesssim 0.115$. In the latter cases, the trimer became unstable upon a volume reduction because the central part of liquid-vapor undergoes a sudden burst instability. In the majority of cases the final state attained after the snap–in instability at $s_{12} > 0.12$ is a pendular bridge dimer. In contrast to the snap–in instability, burst instabilities occur for small gap openings $s_{12} < 0.12$, only, and lead to a final state of three pendular bridges.

For a quantitative comparison of the trimer instabilities observed in different experimental realizations and our numerical energy minimizations, it is useful to consider the mean curvature H of the liquid-vapor interface at the onset of the instability leading to the decay of the trimer. To this end we extracted the projected shape of the menisci of the coalesced pendular bridges spanning the pair of beads that are in contact. Because the outer parts of these interfaces are hardly affected by the liquid in the throat connecting the pendular bridges, the projected contours of these menisci are still close to the shape of an isolated pendular bridge. Adopting the toroidal approximation of pendular bridges for these menisci, we fit the in–plane contour of the outer menisci by circular arcs. The mean curvature H of the interface is the arithmetic mean $H = (\kappa_{\parallel} + \kappa_{\perp})/2$ of the in-plane ($\parallel$) and out-of-plane ($\perp$) curvatures $\kappa_{\parallel} = 1/r_{\parallel}$ and $\kappa_{\perp} = 1/r_{\perp}$, respectively. Here, $r_{\parallel}$ is the radius of the fitted arc while $r_{\perp}$ denotes the distance of the outer meniscus from the respective contact of the bead pair. This geometrical analysis of the liquid interface is done only on the last video frame that still shows a complete trimer, or before the outer meniscus in the gap accelerated while approaching the snap–in instability.

Figure 6 (c) displays the values of the mean curvature H estimated in our experiments for various gap openings s_{12}. In comparison to the experimental data, we plot in Fig. 6 (c) the corresponding values of the mean curvature obtained in our numerical energy minimizations. A transition between the snap–in and the burst instability is clearly visible as a kink in both the experimental and the numerical data. A small systematic shift in the mean curvature between the experimental data points and the numerical results is apparent in the plot of Fig. 6 (c), but the numerical data fall into the range of the experimental uncertainties. Our experimental data show a cross-over between the burst and the snap–in instability for a gap opening $s_{12} \approx 0.12$. This value coincides perfectly with the numerically determined value where we assumed a material contact angle of $\theta_0 = 5°$.

C. Capillary forces

After discussing the possible liquid states and their interfacial instabilities in Sec. III A and Sec. III B, we will now turn to the capillary forces on the beads in contact to the liquid. It is evident that the total capillary force acting on a single bead in the presence of three pendular bridges is a sum two central forces. But also for the trimer/dimer morphology, the total forces $\mathbf{F}_i$ acting on bead i can be decomposed into a pairs of central forces, as illustrated in Fig. 2. Such a decomposition is always possible for three spherical beads whose center points are not co-linear. The proof is given in the Appendix IV B. Due to the reflection symmetry of the bead configuration, the magnitude of the pair forces F_{ij} with $i, j \in \{1, 2, 3\}$ are invariant upon interchanging bead 1 by bead 2. Hence, the capillary forces satisfy $F_{13} = F_{23}$, and we need to consider only two independent forces, the force F_{12} acting across the gap and the force F_{13} acting at one of the two contacts.

1. *Three pendular bridges*

Figure 7 (a) and (b) illustrates the capillary forces acting in a symmetric bead configuration with a finite gap opening $s_{12} > 0$ and $s_{13} = s_{23} = 0$ in the presence of three pendular bridges with total volume V. As already mentioned in the beginning of Sec. III A, we assume a mutual exchange of liquid volume between the bridges. The Laplace pressure P of the bridges as a function of gap opening s_{12} and total volume V is shown in Fig. 7 (c).

The dashed lines in Fig. 7 indicate the region (s_{12}, V) where configurations of three pendular bridges are mechanically stable. Once the stability limit is reached during an adiabatically slow change of s_{12} and V, the bridge ensemble will become unstable and decay into an interfacial morphology with a lower interfacial free energy. For small total volumes V below the asterisk symbol in Fig. 7, the ensemble of three pendular bridges becomes unstable with respect to a mutual exchange of volume. In the course of this instability, the pendular bridge located at gap will be spontaneously 'sucked up' by the two bridges at the contacts. In the upper part of the stability limit above the symbol, we observe that the contact lines of at least one pair of bridges touch, followed by coalescence.

Inspection of Fig. 7 (a) shows that the attractive force

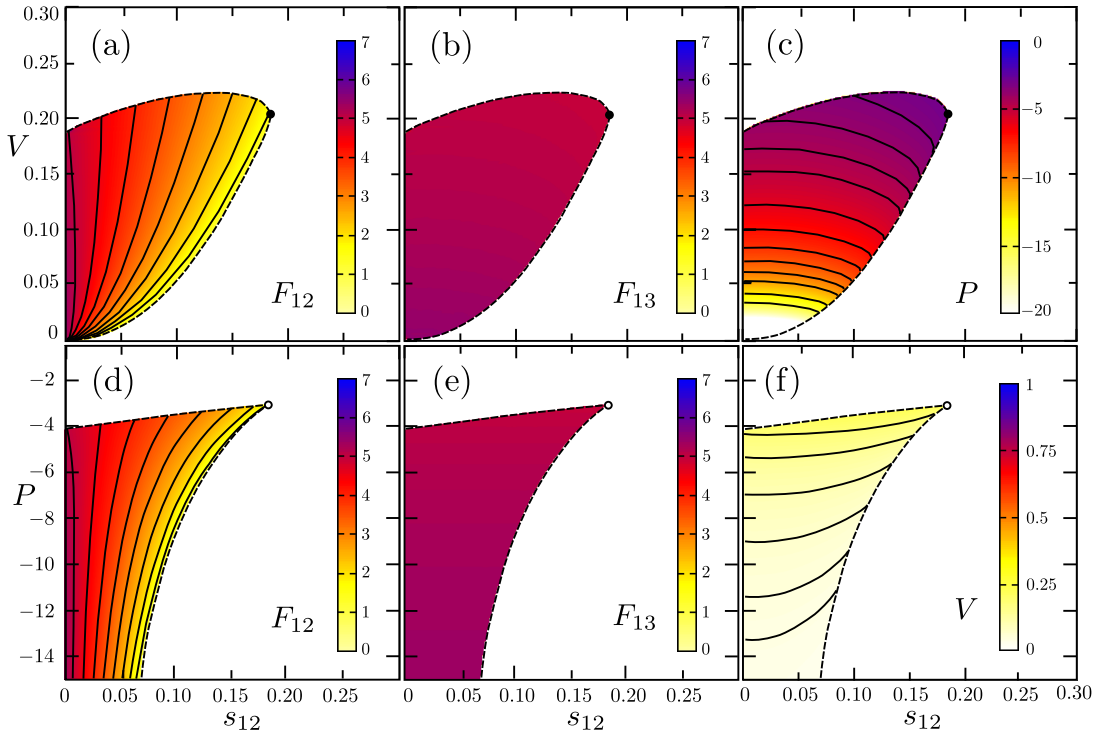

FIG. 7. (Color online) Attractive capillary forces F_{12} across the gap (a) and F_{13} at the contact (b) in presence of three pendular bridges as a function of the gap opening s_{12} and liquid volume V. Capillary forces F_{12} and F_{13}, and volume V of three pendular bridges in the pressure controlled case are shown in panels (c), (d), and (f), respectively, as function of s_{12} and P.

F_{12} acting across the gap at a fixed total volume V of the bridges varies strongly with the gap opening s_{12}, dropping from a value $F_{12} \approx 5$ at $s_{12} = 0$ to $F_{12} \approx 0$ at the gap opening $s_{12} = s_{12}^*$ on the stability limit for the given volume V. The values of F_{12} at the point $s_{12} = 0$ and $s_{12} = s_{12}^*$ are rather insensitive with respect to changes in V, cf. Fig. 7. As expected, the force F_{12} for a vanishing gap opening $s_{12} = 0$ increases slightly with decreasing V, and only approaches the value $2\pi \cos\theta_0 \approx 6.23$ in the asymptotic limit $V \to 0$. The value of maximum gap opening s_{12}^*, however, depends strongly on the total volume V.

In contrast to F_{12}, the attractive capillary force F_{13} at the bead contacts shown in Fig. 7 (b) does not display a significant variation with neither the gap opening s_{12} nor the total volume V. As expected from the force F_{12} at $s_{12} = 0$, we obtain values $F_{13} \approx 5.5$ with a slight increase to ≈ 6.23 in the asymptotic limit $V \to 0$. The Laplace pressure P of three communicating pendular bridges in Fig. 7 (c) depends on both control parameters, s_{12} and V. Apparently, the dependence of P on V is more pronounced than the dependence on s_{12}.

In many instances it is appropriate to assume that the clusters in the wet granular assembly exchange liquid with neighboring structures [12, 18, 20]. Here, one may regard the average Laplace pressure of the neighboring structures as the relevant control parameter. In the latter case, we need to consider local minima of the Grand interfacial energy $\mathcal{G}$ rather than local minima of the interfacial energy $\mathcal{E}$.

Capillary forces F_{12} and F_{13} of three pendular bridges in the pressure controlled case are shown in Fig. 7 (d)and (e) as a function of gap opening s_{12} and Laplace pressure P. We find the same cross-over between the decay modes as in the volume controlled case discussed above. For high Laplace pressures P (with negative sign, but with low magnitude), the pendular bridges are unstable with respect to coalescence while for small values of P (i.e. with negative sign, and large magnitude), the bridge at the gap becomes unstable with respect to a volume exchange with the reservoir. The corresponding stability limit in Fig. 7 is shown as a dashed line where the symbol indicates the cross-over between the two modes of instability.

Similar to the volume controlled case, the force F_{12} acting across the gap decays with increasing gap opening s_{12}, cf. Fig 7 (d). At a fixed gap opening s_{12}, the capillary forces become stronger with a decreasing Laplace pressure P (i.e. with negative sign and increasing magnitude), reaching the asymptotic value $2\pi \cos\theta \approx 6.23$ for $s_{12} = 0$ only in the limit $P \to -\infty$. Close to the segment of the stability boundary related to bridge coalescence, we find $F_{12} \approx 5$, similar to the values in the volume controlled case at large V. Figure 7 (e) displays the capillary force at the bead contacts, F_{13}, which is insensitive with respect to P, and with a similar values in the range $F_{13} \approx 5$

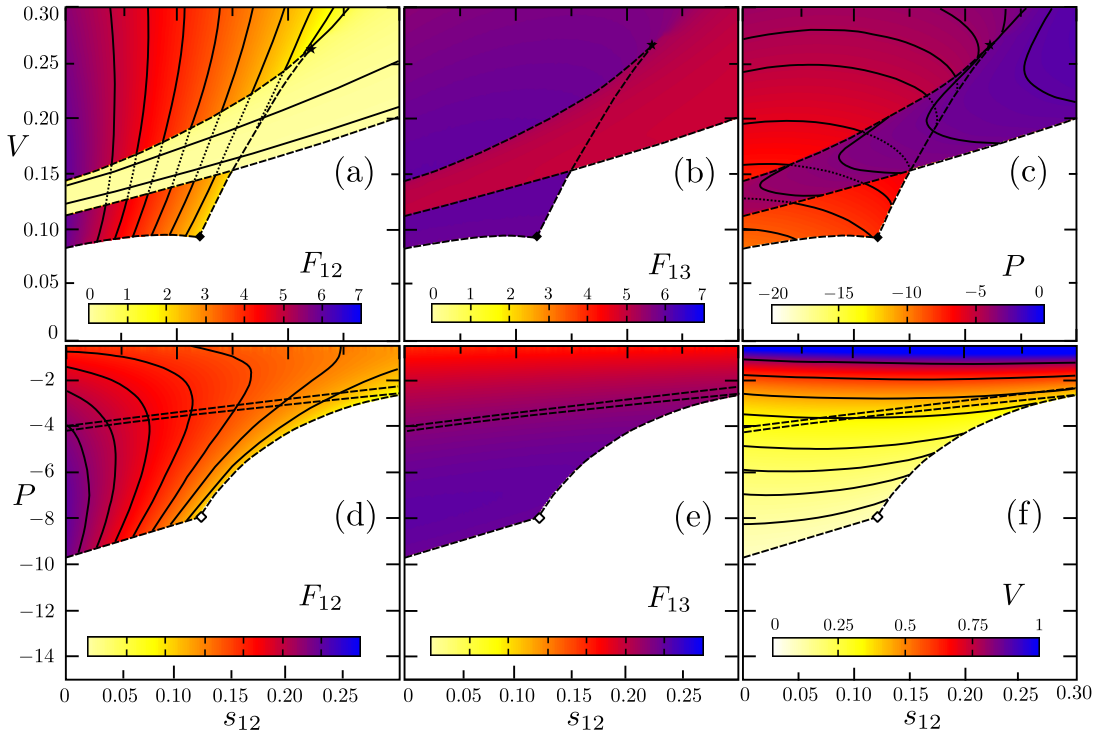

FIG. 8. (Color online) Attractive capillary forces F_{12} across the gap (a), F_{13} at the contact (b), and Laplace pressure P of trimer/dimer (c) as a function of the gap opening s_{12} and liquid volume V. In regions of trimer/dimer bistability, the forces of the morphology with the smaller meniscus distance d is displayed, cf. also the diagram in Fig. 5. Capillary forces F_{12} and F_{13}, and volume V of a trimer/dimer morphology in the pressure controlled case are shown in panels (d), (e), and (f), respectively, as function of s_{12} and P .

close to the coalescence line. The total volume V of the three bridges is shown the last panel of Fig. 7 (f).

2. *Trimer/dimer morphology*

In the following we will discuss the capillary forces of the trimer/dimer morphology in the volume and pressure controlled cases. Figure 8 (a) and (b) display the magnitude of the attractive capillary forces F_{12} and F_{23} In regions of the control parameter gap opening s_{12} and liquid volume V related to a morphological bistability, i.e. where both the dimer and the trimer are locally stable shapes, the map displays the forces corresponding to the liquid conformation with the larger value of the order parameter d, which is the trimer.

In contrast to a trimer a dimer exerts a very small attractive force F_{12} across the gap as expected from the liquid distribution between the beads. The attractive force F_{12} in presence of a trimer depends strongly on the gap opening s_{12} but only weakly on the volume V, while its magnitude is much larger than that of a dimer. Only small variations of the capillary force F_{13} at the two contacts is observed with respect to variations of the gap opening s_{12}. The attractive force F_{13} with a value around 6 hardly depends on the volume V and is not far from the asymptotic value $2\pi\cos\theta_0 \approx 6.23$ for pendular bridges between two spherical beads for $s_{12} = 0$ in the limit $V \to 0$. Similar to the trimer, the dimer exerts rather constant forces between the spherical beads in contact which is approximately $F_{13} \approx 5$, i.e. less than the capillary force in presence of a trimer with the identical volume.

Figure 8 (c) displays the Laplace pressure P of the dimer/trimer morphology. The Laplace pressure mainly depends on the liquid volume V and only weakly on the gap opening s_{12}. Note, that dimers display a larger Laplace pressure (i.e. negative with a smaller magnitude) as compared to a trimer at the same volume. A transfer of liquid from the outer menisci of the dimer into the central region of the throat is accompanied by a decrease of volume in the outer menisci. The redistribution of liquid volume leads to a decrease of the mean curvature and, hence, to a decrease of the Laplace pressure. Note, that the Laplace pressure of a trimer is typically negative but may become positive for large volumes.

Figure 8 (d) and (e) display the capillary force F_{12} at the gap and F_{13} at the contacts for liquid morphologies in the plane spanned by the gap opening s_{12} and Laplace pressure P. It is apparent that the region in (s_{12}, P)-plane where the dimer/trimer morphology exists as a local minimum of the Grand interfacial free energy displays a shape similar to the region in the volume controlled case. As expected, the 'burst' and the snap–in

instability modes form a kink in the stability limit of the trimer at the point $(s_{12}^{\diamond}, P^{\diamond}) = (0.12, -8.0)$. The two almost parallel dashed lines in the upper region of the color plots indicate the narrow region where dimers can exist as metastable configurations in the pressure controlled case. As in the volume controlled case, trimers can decay either by the snap–in of the liquid menisci at the sides or by a burst instability leading to an opening of the throat. The pressure at the latter instability linearly increases with the gap opening s_{12}, and the curve $P(s_{12})$ terminates together with the lines of the snap–in and the pop–out instability in a point $(s_{12}^{\diamond}, P^{\diamond}) = (0.12, -8.5)$. At this point, the stability boundary of the trimer exhibits a kink. The stability boundaries corresponding to the snap–in and pop–out instabilities join smoothly in a cusp bifurcation point at $(s_{12}^{*}, P^{*}) = (0.4, -2.3)$ which lies outside the range shown in the Fig. 8(d) to (f).

The capillary force F_{12} acting across the gap in the presence of a trimer displays a strong dependence on the gap opening s_{12}. However, the magnitude of F_{12} varies only weakly with the Laplace pressure P. A stronger dependence is observed only above a value of $P \approx -4.5$, at a point where the trimer itself would have already fused with other neighboring liquid structures (bridges or trimer) inside the random assembly of spherical beads [12, 20]. The capillary force F_{12} at the gap created by the trimer is approximately by a factor 1.1 larger than the capillary force of a single bridge at a prescribed Laplace pressure of $P = -4.5$ at the same distance s_{12}.

Figure 8 (e) reveals that the capillary force F_{13} at the contacts depends on the magnitude of the Laplace pressure P, while F_{13} is virtually constant with respect to the gap opening s_{12}. Also in this case, the capillary force is approximately by a factor ≈ 1.1 larger than the force for a single pendular bridge at the contact held at the same value of $P = -4.5$. The liquid volume V of a trimer in the pressure controlled case depends to a larger degree on the magnitude of P and only weakly on the gap opening s_{12}, cf. the color plot in Fig. 8 (f). An analogous statement applies to an ensemble of three isolated pendular bridges that are allowed to exchange liquid.

Simulations of the mechanics and dynamics of large wet granular assemblies require efficient models for capillary cohesion. At low liquid saturations, in the regime of pendular bridges, the cohesive force can be treated as a superposition of two–body forces. For saturations in the funicular regime, a simple mapping of the capillary cohesion forces onto an equivalent ensemble of pendular bridges would be desirable. In the most simple approach, one would assume that the magnitude of capillary forces caused by the trimer/dimer are similar to those in the presence of three pendular bridges for the same volume or Laplace pressure.

Figure 9 (a) and (b) provides a quantitative comparison of the stability boundaries of three pendular bridges to the ones of the trimer/dimer morphology in the volume controlled and the pressure controlled cases, respectively. Figure 9 (c) and (d) display the capillary force at the gap for three pendular bridges and the trimer/dimer morphology as a function of the gap opening. As we are plotting the capillary force F_{12} and F_{13} in the volume controlled and the Laplace pressure controlled case in the same plot as a function, we chose specific values of volume V and Laplace pressure P. For these particular values the morphologies and, hence, the capillary forces are identical at zero gap opening $s_{12} = 0$.

Figure 9 (c) and (d) clearly demonstrate that a trimer induces a higher attractive force across the gap. In addition, the snap–in transition from trimer to dimer occurs at a larger gap opening as compared to the point where the bridge at the gap decays in a ensemble of three communicating bridges.

IV. CONCLUSION AND OUTLOOK

In this article we have explored the morphology and capillary forces of a pendular bridge trimer representing the most fundamental liquid cluster in disordered assemblies of wet spherical beads. We have focused our study on local triangular bead configurations with two contacts and one finite gap. Numerical minimizations of the interfacial energy reveal a shape bistability between a dimer and a trimer of pendular bridges. Such a capillary hysteresis between the trimer and the dimer shapes is present both in the volume and in the Laplace pressure controlled cases. As the gap opening is changed, we find a cross–over between two different interfacial instabilities that can occur during a quasi-static volume reduction. At small gap openings the two opposing menisci in the triangular throat touch and break up in a sudden burst. For intermediate gap openings, however, the timer decays by a sudden, discontinuous snap–in of the meniscus in the gap once the meniscus is close to the narrowest point. A continuous motion of the meniscus is observed in wide gaps. Systematic evaporation experiments in the geometry of three beads with a single finite gap opening quantitatively reproduce the transition from a snap–in and a burst instability of a trimer as the gap opening is decreased.

In respect to the modeling of the attractive capillary forces, it is well justified to replace the bridge dimer by two separate pendular bridges which are held at the same Laplace pressure as the dimer. Bridge trimers, however, induce attractive capillary forces across the gap that are slightly larger than the force of a pendular bridge at the gap for the same Laplace pressure. The rupture distance of the pendular bridge at the gap is systematically larger than the gap opening where the snap–in transition from trimer to dimer occurs. Hence, trimers of pendular bridges not only yields to an increased cohesion between the beads but also the range over which the increased capillary force act is enlarged. Both effects lead to a enhanced dissipation of work during a slow deformation

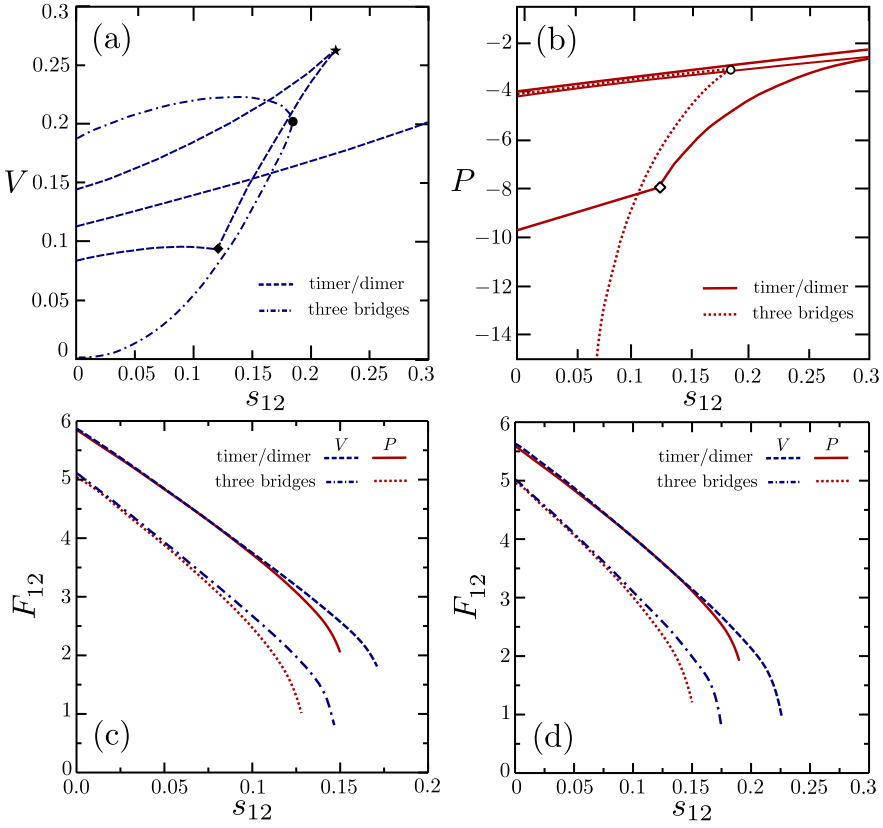

FIG. 9. (Color online) Comparison of the stability boundaries of a trimer/dimer morphology and of three pendular bridges in terms of the gap opening s_{12} and (a) the total liquid volume V in the volume controlled case or (b) the Laplace pressure P in the pressure controlled case. (c): capillary force F_{12} at the gap as a function of gap opening s_{12}. Shown are data for three pendular bridges at a fixed total volume $V = 0.116$ (dashed-dotted lines) and for a fixed Laplace pressure $P = -6$ (dotted line) in comparison to Data for the trimer morphology at a fixed volume $V = 0.190$ (dashed line) and for a fixed Laplace pressure $P = -6$ (solid line). (d): Data for three pendular bridges of fixed total volume $V = 0.1644$ (dashed-dotted line) and for a fixed Laplace pressure $P = -4.5$ (dotted line) in comparison to data for a trimer at fixed volume $V = 0.264$ (dashed line) and for a fixed Laplace pressure $P = -4.5$ (solid line).

of a granular assembly. These two observation may already be sufficient to explain the shallow maximum of the strength of wet granulates reported in experiments [12, 20].

ACKNOWLEDGMENTS

The authors would like to thank R. Mani, D. Kadau, and H.-J. Herrmann for fruitful discussions. This work has been funded by the German Science Foundation (DFG) within the SPP 1486 'PiKo' under Grant No. HE 2016/14-2.

APPENDIX

A. Equivalence of capillary forces

Respecting the sign convention of the Laplace pressure, we find the identity

$$P = \tilde{P}(\bar{\mathbf{r}}, V) = \partial_V E(\bar{\mathbf{r}}, V) \ . \tag{12}$$

Starting from the definition (2) of the Grand interfacial free energy $\mathcal{G}$ and differentiation with respect to the coordinates $\bar{\mathbf{r}}$ and using eqn. (12) we obtain the following identity:

$$\nabla_{\mathbf{r}_i} G\big(\bar{\mathbf{r}}, P\big) = \nabla_{\mathbf{r}_i} E\big(\bar{\mathbf{r}}, \tilde{V}(\bar{\mathbf{r}}, P)\big) - P\, \nabla_{\mathbf{r}_i} \tilde{V}\big(\bar{\mathbf{r}}, P\big) \ . \tag{13}$$

By the chain rule of differentiation, we can write the first term in eqn. (13) as

$$\begin{aligned} \nabla_{\mathbf{r}_i} E\big(\bar{\mathbf{r}}, \tilde{V}(\bar{\mathbf{r}}, P)\big) &= \nabla_{\mathbf{r}_i} E\big(\bar{\mathbf{r}}, V\big)|_{V=\tilde{V}(\bar{\mathbf{r}},P)} \\ &+ \partial_V E(\bar{\mathbf{r}}, V)|_{V=\tilde{V}(\bar{\mathbf{r}},P)} \nabla_{\mathbf{r}_i} \tilde{V}\big(\bar{\mathbf{r}}, P\big) \ , \end{aligned} \tag{14}$$

and using the expression eqn. (12) for the Laplace pressure, we finally obtain

$$\nabla_{\mathbf{r}_i} G\big(\bar{\mathbf{r}}, P\big) = \nabla_{\mathbf{r}_i} E\big(\bar{\mathbf{r}}, V\big)|_{V=\tilde{V}(\bar{\mathbf{r}},P)} \ , \tag{15}$$

which proofs the equivalence of capillary forces in the volume and pressure ensembles.

B. Decomposition of forces

First, we will consider the case of three identical beads whose centers are not co-linear, i.e. $\mathbf{r}_{12} \times \mathbf{r}_{13} \neq \mathbf{0}$ where $\mathbf{r}_{ij} \equiv \mathbf{r}_i - \mathbf{r}_j$ are the relative positions of the bead centers $\mathbf{r}_i$, $i \in \{1,2,3\}$. The co-linear case will be discussed separately.

Employing the unit vector $\mathbf{n}_{ij}$ pointing from the center of bead i to the center of bead j, and the unit vector $\mathbf{n}^\perp$ given by

$$\mathbf{n}^\perp = \frac{\mathbf{r}_{12} \times \mathbf{r}_{13}}{|\mathbf{r}_{12} \times \mathbf{r}_{13}|} \ , \tag{16}$$

we can decompose the forces $\mathbf{F}_i$ onto bead i into a sum of forces

$$\sum_{\substack{i=1 \\ j\neq i}}^{3} F_{ij}\mathbf{n}_{ij} + F_i^\perp \mathbf{n}^\perp = \mathbf{0} \tag{17}$$

with $j \in \{1,2,3\}$ and $j \neq i$. To proof the conjecture that the three body force can be written as sum over central force pairs, we now have to show that $F_{ij} = -F_{ji}$ as well as $F_i^\perp = 0$ holds for all $i,j \in \{1,2,3\}$. We start our proof with the observation that the total torque on the beads vanishes:

$$\sum_{i=1}^{3} \left(\mathbf{r}_i \times \mathbf{F}_i + \mathbf{T}_i\right) = \mathbf{0} \ . \tag{18}$$

Under the assumption that $\mathbf{T}_i = \mathbf{0}$ for $i \in \{1,2,3\}$, we are left with the identity

$$\sum_{i=1}^{3} \mathbf{M} \cdot \left[\, \mathbf{F}_i \times (\mathbf{r}_i - \mathbf{r}_0)\right] = 0 \tag{19}$$

for an arbitrary rotation axis $|\mathbf{M}| = 1$ and center of rotation, $\mathbf{r}_0$, because all forces $\mathbf{F}_i$ with respect to the centers of the beads must sum to zero. Without restricting generality, we chose the center $\mathbf{r}_0 \equiv \mathbf{r}_1$ and a direction $\mathbf{M} \equiv \mathbf{n}^\perp$ of the axis. Equation (19) can be now rewritten as

$$\begin{aligned} \mathbf{n}^\perp \cdot [&(F_{23}\,\mathbf{n}_{23} + F_2^\perp\,\mathbf{n}^\perp) \times \mathbf{r}_{13} \\ &(F_{32}\,\mathbf{n}_{32} + F_3^\perp\,\mathbf{n}^\perp) \times \mathbf{r}_{12}] = 0 \ . \end{aligned} \tag{20}$$

By the definition of the unit vectors $\mathbf{n}^\perp$ and $\mathbf{n}_{23} = -\mathbf{n}_{32}$, we have $\mathbf{n}^\perp \cdot \mathbf{n}_{ij} = 0$ and

$$\mathbf{n}_{23} \times \mathbf{r}_{13} = -\mathbf{n}_{32} \times \mathbf{r}_{12} = \frac{2\,A_\Delta}{|\mathbf{r}_{23}|}\,\mathbf{n}^\perp \ , \tag{21}$$

where A_Δ is the area of the triangle defined by the three bead centers. With eqn. (21) and eqn. (20), we arrive at $F_{23} = -F_{32}$. The choice of bead indices was arbitrary which implies that also $F_{12} = -F_{21}$ and $F_{13} = -F_{31}$ must hold.

In order to show $F_1^\perp = F_2^\perp = F_3^\perp = 0$, we chose the rotation axis in the plane of the three bead centers, passing through the center of bead 1. The direction of the rotation axis is given by

$$\mathbf{M} \equiv \frac{\mathbf{r}_{21} + \mathbf{r}_{31}}{|\mathbf{r}_{21} + \mathbf{r}_{31}|} \tag{22}$$

and $\mathbf{r}_0 \equiv \mathbf{r}_1$. With this choice, the torque acting on the beads has to satisfy

$$\frac{(\mathbf{r}_{21} + \mathbf{r}_{31}) \times \mathbf{n}^\perp (F_2^\perp - F_3^\perp)}{|\mathbf{r}_{21} + \mathbf{r}_{31}|} = 0 \tag{23}$$

which gives $F_2^\perp = F_3^\perp$.

Following the same line of arguments for a rotation axis passing through the center of bead 2 and the point $\mathbf{r}_2 + (\mathbf{r}_{12} + \mathbf{r}_{32})/2$, we obtain $F_1^\perp = F_2^\perp$. Since the sum of over all forces $\mathbf{F}_{ij}$ in the plane of the three bead centers vanishes, also all normal forces must sum to zero, leaving as the only possibility $F_1^\perp = F_2^\perp = F_3^\perp = 0$.

In the case of three co-linear bead centers, a unique decomposition into three central force pairs must not necessarily be possible. A simple counterexample are forces $\mathbf{F}_1 = \mathbf{F}_3$ and $\mathbf{F}_2 = -2\,\mathbf{F}_1$, all orthogonal to the line, distances $\mathbf{r}_{12} = \mathbf{r}_{32}$ where bead 2 is located halfway in between beads 1 and 3. The singular nature of this case can be easily seen when approaching the co-linear configuration from a configuration with a slight bend in the plane of the forces. If there is no spontaneous symmetry breaking of the liquid shape, all capillary forces must act parallel to line passing through the bead centers which, again, allows a unique decomposition into force pairs.

[1] W. B. Haines, Studies in the physical properties of soils. II. A note on the cohesion developed by capillary forces in an ideal soil. J. Agric. Sci. 15,529 (1925).

[2] R. A. Fisher, On the capillary forces in an ideal soil. J. Agric. Sci. 16,492 (1926).

[3] T. Gillespie and W. J. Settineri, The Effect of Capillary Liquid on the Force of Adhesion between Spherical Solid Particles, Journal of Colloid and Interface Science 24, 199

(1967).
[4] K. Hotta, K. Takeda, and K. Iinoya, The capillary binding force of a liquid bridge. Powder Technology 10,231 (1974).
[5] F. M. Orr, L. E. Scriven, and A. P. Rivas, Pendular rings between solids: meniscus properties and capillary force, Journal of Fluid Mechanics 67,723 (1975).
[6] G. Lian, C. Thornton C, and M. J. Adams, A theoretical study of the liquid bridge forces between two rigid spherical bodies, Journal of Colloid and Interface Science 161,138 (1993).
[7] C.D. Willett, M.J. Adams, S.A. Johnson, and J.P.K. Seville, Capillary Bridges between Two Spherical Bodies, Langmuir 16,24 (2000).
[8] M. Dormann and H. J. Schmid, Simulation of capillary bridges between nanoscale particles, Langmuir 30,1055 (2014).
[9] V. Richefeu, M. S. El Youssoufi, and F. Radjaï, Shear strength properties of wet granular materials, Phys. Rev. E 73,051304 (2006)
[10] R. Mani, D. Kadau, D. Or, and H.J. Herrmann, Fluid depletion in shear bands, Phys. Rev. Lett. 109,248001 (2012).
[11] H.-J.Butt and M. Kappl, Normal capillary forces, Advances in Colloid and Interface Science 146,48 (2009).
[12] M. Scheel et al., Morphological clues to wet granular pile stability, Nature Materials 7,189 (2008).
[13] N. Mitarai and F. Nori, Wet granular materials, Advances in Physics 55,1 (2006).
[14] S. Herminghaus. *Wet Granular Matter, A Truly Complex Fluid*, vol. 6 of *Series in Soft Condensed Matter*. World Scientific, Singapur, 2013.
[15] K. Melnikov et al., Grain-scale modeling of arbitrary fluid saturation in random packings, Phys. Rev. E 91,042204 (2015).
[16] T. C. Halsey and A. J. Levine, How Sandcastles Fall, Phys. Rev. Lett. 80,3141 (1998).
[17] R. Turton, Challenges in the modeling and prediction of coating of pharmaceutical dosage forms. Powder Technology, 181, 186 (2008).
[18] R. Mani et al., Role of contact-angle hysteresis for fluid transport in wet granular matter, Phys. Rev. E 91,042204 (2015)
[19] S. Herminghaus, Dynamics of wet granular matter, Advances in Physics 54,221 (2005).
[20] M. Scheel et al., Liquid distribution and cohesion in wet granular assemblies beyond the capillary bridge regime, J. Phys.: Condens. Matter 20:494236 (2008).
[21] C. C. Harris and N. R. Morrow, Pendular Moisture in Packings of Equal Spheres, Nature 203,706 (1964).
[22] J. L. Finney, Random Packings and the Structure of Simple Liquids. I. The Geometry of Random Close Packing, Proc. R. Soc. London, A 319,479 (1970).
[23] Gravity or buoyancy is taken into account by the energy term $\Delta\rho\, g\, z_{\rm cm}$, where $\Delta\rho \equiv \rho^{\rm l} - \rho^{\rm v}$ is the density difference between the liquid and the vapor phase, g the acceleration of gravity, and $z_{\rm cm}$ the vertical center of mass position of the liquid body.
[24] M. do Carmo, *Differential Geometry of Curves and Surfaces*, Prentice Hall, 1976.
[25] A. Thom, *Structural Stability and Morphogenesis – an outline of a general theory of models*. Addison-Wesley, 2. edition, 1989.
[26] V.I. Arnold, *Catastrophe Theory*. Springer, 3. edition, 2003.
[27] K. Brakke, The Surface Evolver, Exp. Math. 1:141, 1990.